

# Benchmarking the Scrape-Off-Layer Fast Ion (SOLFI) particle tracer code in a collisionless magnetic mirror with electrostatic potential drop

X. Zhang,<sup>1,\*</sup> N. A. Lopez,<sup>1</sup> and F. M. Poli<sup>2</sup>

<sup>1</sup>*Department of Astrophysical Sciences, Princeton University, Princeton, New Jersey 08544, USA*

<sup>2</sup>*Princeton Plasma Physics Laboratory, Princeton, New Jersey, 08543, USA*

Optimizing the confinement and transport of fast ions is an important consideration in the design of modern fusion reactors. For spherical tokamaks in particular, fast ions can significantly influence global plasma behavior because their large drift orbits often sample both core and scrape-off-layer (SOL) plasma conditions. Their Larmor radii are also comparable to the SOL width, rendering the commonly chosen guiding center approximations inappropriate. Accurately modeling the behavior of fast ions therefore requires retaining a complete description of the fast ion orbit including its Larmor motion. Here, we introduce the Scrape-Off-Layer Fast Ion (SOLFI) code, which is a new and versatile full-orbit Monte Carlo particle tracer being developed to follow fast ion orbits inside and outside the separatrix. We benchmark SOLFI in a simple straight mirror geometry and show that the code (i) conserves particle energy and magnetic moment, (ii) obtains the correct passing boundary for particles moving in the magnetic mirror field with an imposed electrostatic field, and (iii) correctly observes equal ion and electron current at the ambipolar potential predicted from analytical theory.

## I. INTRODUCTION

Spherical Tokamaks (STs) are an attractive design option for a fusion reactor that promises significant cost reduction because of its compact size and denser confined plasmas [1–4]. However, there are still open questions regarding ST physics, particularly regarding the physics of fast ions that are produced through fusion reactions or neutral beam injection (NBI) [5, 6]. These fast ions are an important particle, momentum, and energy source for the core plasma [7–11]. They also influence the plasma macroscopic stability through excitation of Alfvén eigenmodes [12–16], and through strong interaction with MHD activities [10, 17–19]. Because of the interplay between their large orbit sizes and the high mirror ratio inherent to the low aspect ratio ST magnetic geometry, fast ions in STs possess unique transport properties that can be difficult to simulate [20].

Recently there has also been an increased interest in the lithium conditioning of plasma-facing components (PFCs) as a means to better handle the divertor heat flux in reactor-grade tokamaks [21–27]. These lithium-coated PFCs (Li-PFCs) have also been shown to greatly improve the core confinement properties, to reduce oxygen impurity concentration, and to suppress damaging edge-localized modes [28–31]. The use of Li-PFCs also has implications for fast ion physics because Li-PFCs reduce the edge neutral recycling, which in turn increases the temperature and decreases the density of the plasma in the scrape-off-layer (SOL) region [32–38]. The neo-classical collisionality of the SOL is thus greatly reduced, and fast ions can readily exhibit orbits that return to the core after crossing the separatrix into the SOL. The accurate modelling of such orbits requires a versatile particle

tracer that can follow the fast ion orbits in both the core and the SOL plasma.

Since the temperature and density scale length in the SOL plasma is often comparable to the typical fast ion Larmor radius [39, 40], a full-orbit code is needed to accurately simulate the fast ion orbits in the SOL. Therefore, the 3-D full-orbit Monte Carlo code called the Scrape-Off-Layer Fast Ion (SOLFI) code is currently under development as a possible means to extend the modeling capabilities of the NBI code NUBEAM [41] into the SOL. In this work, we benchmark the SOLFI code by simulating the particle losses in a collisionless magnetic mirror, which can be considered a simple approximation of a hot collisionless SOL in a low aspect ratio ST, such as the Lithium Tokamak eXperiment (LTX) [42] and the National Spherical Torus eXperiment Upgrade (NSTX-U) [43]. We derive an analytical expression for the passing particle current for each individual species in the presence of an electrostatic potential drop, and calculate the resulting ambipolar potential that arises from the requirement that the total passing current vanishes. The simulation results are compared with the theoretical predictions to demonstrate the validity of the SOLFI code, which exhibit remarkable agreement.

This paper is organized as follows. In Sec. II we present a simple analytical framework for computing the passing particle current in a straight magnetic mirror field with imposed electrostatic potential, including when the electrostatic potential is ambipolar. In Sec. III, the SOLFI code is introduced and benchmarked on a simple analytical magnetic mirror field, whose derivation is also presented. In particular, the conservation of energy and magnetic moment is demonstrated for both trapped and passing particles, and the analytical prediction for the ambipolar potential derived in Sec. II is verified. Finally, in Sec. IV we summarize our main results. Auxiliary calculations are presented in two appendices.

\* Corresponding author: xz5@princeton.edu

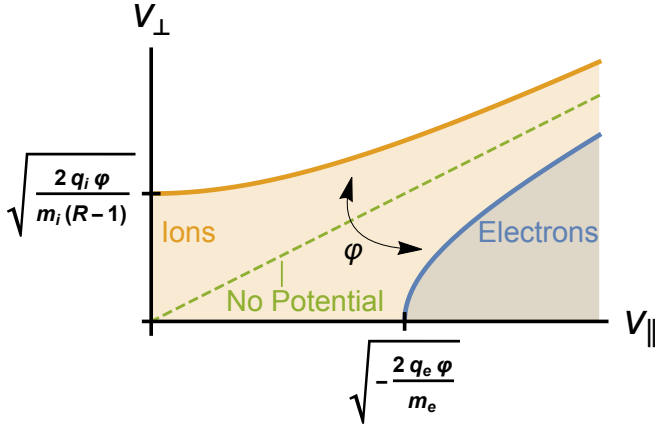


**FIG. 1:** The passing region (shaded color) of midplane velocities  $v_\perp$  and  $v_\parallel$  for a magnetic mirror with mirror ratio  $R$  and electrostatic potential drop  $\phi$ . The passing region is given explicitly by Eq. 7, which can also be written as  $v_\perp \leq \sqrt{(v_\parallel^2 + 2q_s\phi/m_s)/(R-1)}$ ; hence, the passing region generally takes the form depicted in the figure for  $\phi \geq 0$ .

## II. LOSS PARTICLE CURRENT AND AMBIPOLAR POTENTIAL DROP IN COLLISIONLESS MIRROR

Let us consider a magnetic mirror field aligned along  $\hat{x}$  in a two-dimensional (2-D) slab geometry with  $\hat{z}$  an ignorable coordinate. Specifically, we take

$$\mathbf{B} = B_x(x, y)\hat{x} + B_y(x, y)\hat{y} \quad (1)$$

such that

$$B_x(x, y) > 0, \quad B_y(x, 0) = 0 \quad (2a)$$

and for any  $x_2 \geq x_1 \geq 0$ ,

$$|\mathbf{B}(x_2, y)| \geq |\mathbf{B}(x_1, y)|. \quad (2b)$$

We assume  $\mathbf{B}$  to be sufficiently strong such that, neglecting collisions, the particle transport is dominated by dynamics along  $\mathbf{B}$ . Let us also introduce a 1-D electrostatic potential  $\phi(x)$ , which can either be externally imposed or be the ambipolar potential that arises from differential transport of electrons and ions. Finally, let us assume that the particle source is such that the distribution function is spatially confined near the mirror axis  $y = 0$  with a fixed velocity profile at  $x = 0$ . Note that this initial condition implies that the particle dynamics are effectively 1-D, with transverse drifts like the curvature drift and the  $E \times B$  drift being negligible.

Suppose we are interested in the current associated with the passing particles at some plane  $x = L$ . For a single particle of species  $s$  initialized on the mirror axis  $y = 0$ , conservation of magnetic moment implies that [44]

$$\frac{v_{\perp,L}^2}{|\mathbf{B}(L, 0)|} = \frac{v_{\perp,0}^2}{|\mathbf{B}(0, 0)|}, \quad (3)$$

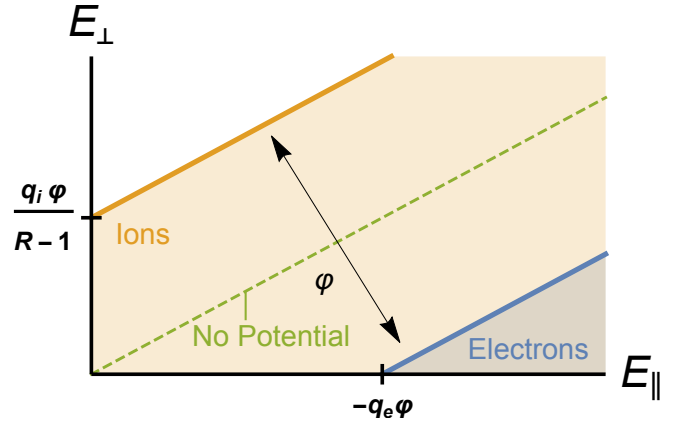


**FIG. 2:** Same as Fig. 1 but for midplane energies  $E_\perp = m_s v_\perp^2/2$  and  $E_\parallel = m_s v_\parallel^2/2$ . In these variables, the passing region (shaded) is simply  $E_\perp \leq (E_\parallel + q_s\phi)/(R-1)$ .

while conservation of energy implies that

$$v_{\parallel,L}^2 + v_{\perp,L}^2 + \frac{2q_s}{m_s}\phi(L) = v_{\parallel,0}^2 + v_{\perp,0}^2 + \frac{2q_s}{m_s}\phi(0). \quad (4)$$

Here,  $m_s$  and  $q_s$  are respectively the mass and charge of species  $s$ , while  $v_{\perp,x}$  and  $v_{\parallel,x}$  denote respectively the perpendicular and parallel components of the particle velocity with respect to the magnetic field at position  $x$ .

Combining Eqs. 3 and 4 yields an expression for the exit velocity  $v_{\parallel,L}$  in terms of the midplane velocities  $v_{\parallel,0}$  and  $v_{\perp,0}$  as

$$v_{\parallel,L} = \sqrt{v_{\parallel,0}^2 - (R-1)v_{\perp,0}^2 + \frac{2q_s}{m_s}\phi}, \quad (5)$$

where we have defined the mirror ratio and the potential drop along the mirror axis as respectively

$$R \doteq \frac{|\mathbf{B}(L, 0)|}{|\mathbf{B}(0, 0)|} \geq 1, \quad \phi \doteq \phi(0) - \phi(L). \quad (6)$$

The ‘passing region’ is defined as the region of midplane velocities such that  $v_{\parallel,L}$  is real, namely,

$$v_{\parallel,0}^2 - (R-1)v_{\perp,0}^2 + \frac{2q_s}{m_s}\phi \geq 0. \quad (7)$$

As shown in Fig. 1, this is a region bounded by a hyperbolic curve which either intersects the  $v_{\perp,0}$  axis ( $q_s\phi > 0$ ), the  $v_{\parallel,0}$  axis ( $q_s\phi < 0$ ), or becomes a straight line intersecting the origin ( $q_s\phi = 0$ ). See also Fig. 2 for a depiction of the passing region in midplane-energy space, rather than midplane-velocity space. Note that we require  $x = L$  to be *accessible*, i.e.,  $v_{\parallel,x} \geq 0$  for all  $0 \leq x < L$  if  $v_{\parallel,L} \geq 0$ . This places constraints on the allowed spatial structure of  $\phi(x)$ .

Given the midplane velocity distribution  $f_s(v_{\parallel,0}, v_{\perp,0})$  for species  $s$  (assumed to be gyrotropic for simplicity), the collected current of species  $s$  at  $x = L$  is obtained

simply as the expectation value of Eq. 5:

$$\langle j_{s,L} \rangle = q_s \int \int_{\text{Passing}} dv_{\parallel,0} dv_{\perp,0} f_s(v_{\parallel,0}, v_{\perp,0}) \times \sqrt{v_{\parallel,0}^2 - (R-1)v_{\perp,0}^2 + \frac{2q_s}{m_s}\varphi}, \quad (8)$$

where the integration is taken over the passing region. When the distribution function is a Maxwellian with density  $n_s$  and temperature  $T_s$ , given explicitly as

$$f_s(v_{\parallel,0}, v_{\perp,0}) = n_s v_{\perp,0} \sqrt{\frac{m_s^3}{2\pi T_s^3}} \times \exp\left[-\frac{m_s}{2T_s}(v_{\parallel,0}^2 + v_{\perp,0}^2)\right], \quad (9)$$

then Eq. 8 takes the form

$$\langle j_{s,L} \rangle = q_s n_s \sqrt{\frac{8T_s}{\pi m_s}} \mathcal{I}\left(\frac{q_s}{|q_e|} \frac{T_e}{T_s} \tilde{\varphi}; R\right), \quad (10)$$

where  $\tilde{\varphi} \doteq \frac{|q_e|\varphi}{T_e}$  is the potential drop normalized by the electron thermal energy and the (dimensionless) integral function  $\mathcal{I}(X; R)$  is given as

$$\mathcal{I}(X; R) = \int \int_{\text{Passing}} du dw w \sqrt{u^2 - (R-1)w^2 + X} \times \exp(-u^2 - w^2). \quad (11)$$

In terms of the nondimensionalized velocities  $u$  and  $w$ , the passing region is defined as the region such that

$$\text{Max}\left[0, \sqrt{(R-1)w^2 - X}\right] \leq u < \infty, \quad (12a)$$

$$0 \leq w \leq \sqrt{\frac{u^2 + X}{R-1}}. \quad (12b)$$

Hence,  $\mathcal{I}(X; R)$  can be written explicitly as

$$\mathcal{I}(X; R) = \begin{cases} \int_0^\infty du \int_0^{\sqrt{\frac{u^2 + X}{R-1}}} dw w \sqrt{u^2 - (R-1)w^2 + X} \exp(-u^2 - w^2) & X \geq 0 \\ \int_{\sqrt{|X|}}^\infty du \int_0^{\sqrt{\frac{u^2 - |X|}{R-1}}} dw w \sqrt{u^2 - (R-1)w^2 - |X|} \exp(-u^2 - w^2) & X < 0 \end{cases}. \quad (13)$$

Then, as shown in Appendix A,  $\mathcal{I}(X; R)$  can be simplified as

$$\mathcal{I}(X; R) = \begin{cases} \frac{X}{8} \left[ K_1\left(\frac{X}{2}\right) + K_0\left(\frac{X}{2}\right) \right] \exp\left(\frac{X}{2}\right) - \frac{\sqrt{X(R-1)}}{4} \mathcal{C}(X; R) \exp\left(\frac{X}{2}\right) & X > 0 \\ \frac{1}{4} - \frac{R-1}{4\sqrt{R}} \text{csch}^{-1}(\sqrt{R-1}) & X = 0 \\ \frac{|X|}{8} \left[ K_1\left(\frac{|X|}{2}\right) - K_0\left(\frac{|X|}{2}\right) \right] \exp\left(-\frac{|X|}{2}\right) - \frac{\sqrt{|X|(R-1)}}{4} \mathcal{S}(|X|; R) \exp\left(-\frac{|X|}{2}\right) & X < 0 \end{cases}, \quad (14)$$

where  $K_\nu(X)$  is the modified Bessel function of the second kind [45], and the auxiliary functions  $\mathcal{C}$  and  $\mathcal{S}$  are defined as

$$\mathcal{C}(X; R) = \int_0^\infty dt \cosh\left(\frac{t}{2}\right) \mathcal{D}\left[\sqrt{\frac{X}{R-1}} \cosh\left(\frac{t}{2}\right)\right] \exp\left[-\frac{X}{2} \cosh(t)\right], \quad (15a)$$

$$\mathcal{S}(X; R) = \int_0^\infty dt \sinh\left(\frac{t}{2}\right) \mathcal{D}\left[\sqrt{\frac{X}{R-1}} \sinh\left(\frac{t}{2}\right)\right] \exp\left[-\frac{X}{2} \cosh(t)\right], \quad (15b)$$

with  $\mathcal{D}(z)$  being the Dawson function [45, 46]. In this form,  $\mathcal{I}(X; R)$  can be tabulated for discrete values of  $X$  and  $R$  using standard quadrature and special functions packages for subsequent interpolations. Figure 3(a) shows  $\mathcal{I}(X; R)$  for  $X \in [-5, 10]$  and  $R \in [1, 5]$ .

Often, the potential drop  $\tilde{\varphi}$  is the ambipolar potential that ensures no net current is collected at the mirror exit  $x = L$ . For a two-component plasma, this means  $\langle j_{i,L} \rangle + \langle j_{e,L} \rangle = 0$ , or equivalently for specific case of

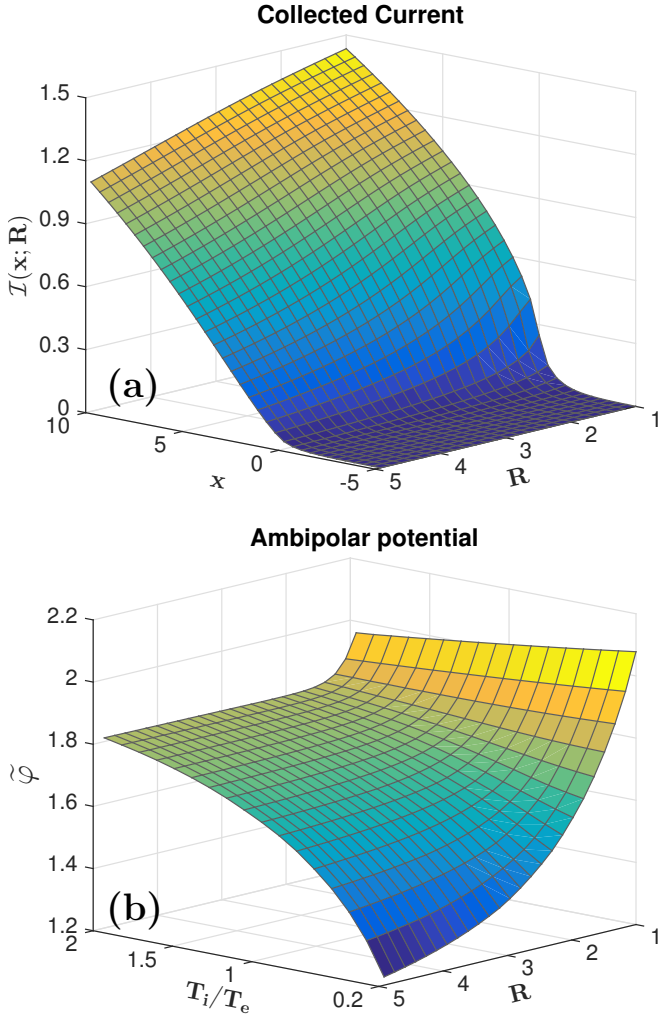


**FIG. 3:** (a) The integral function  $\mathcal{I}(X; R)$ , given explicitly in Eq. 14. (b) Ambipolar potential  $\tilde{\varphi}$  obtained from solving Eq. 16 over the depicted range of temperature ratio and mirror ratio  $R$ .

Maxwellian midplane distributions,

$$\sqrt{\frac{m_e T_i}{m_i T_e}} \mathcal{I}\left(\frac{q_i T_e}{|q_e| T_i} \tilde{\varphi}; R\right) - \mathcal{I}(-\tilde{\varphi}; R) = 0, \quad (16)$$

after using the quasineutrality condition  $q_i n_i = |q_e| n_e$ . The resultant ambipolar potential  $\tilde{\varphi}$  can thus be obtained from Eq. 16 via standard root-finding methods. Figure 3(b) shows the ambipolar  $\tilde{\varphi}$  for Hydrogen plasma for  $T_i/T_e \in [0.2, 2]$  and  $R \in [1, 5]$ .

The dependencies of the ambipolar potential on the mirror ratio as well as ion temperature can be physically understood as follows. When  $R = 1$ , i.e., when there is no magnetic mirror, the ambipolar potential decreases with increasing ion temperature, since the difference between the ion and electron thermal speed decreases with increasing ion temperature. This trend reverses for  $R > 1$ , however, where increasing the ion temperature increases the ambipolar potential. This seemingly counter-intuitive result arises because the passing

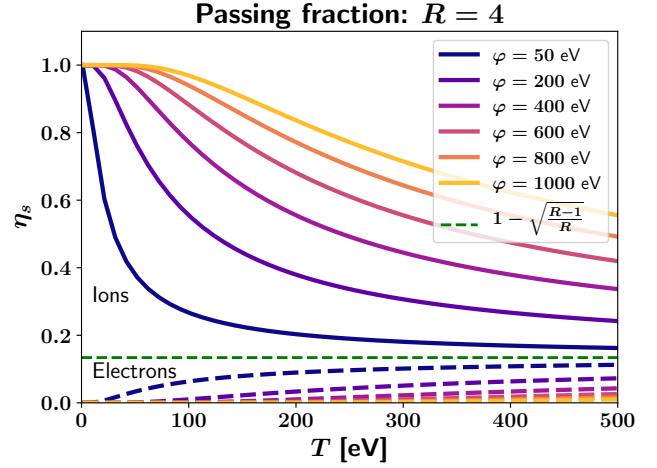


**FIG. 4:** Passing particle fraction  $\eta_s$  for ions (solid lines) and electrons (dashed lines) in a magnetic mirror with  $R = 4$  and various potential drops as the temperature is varied. The ion passing fraction is calculated with Eq. B4, while the electron passing fraction is calculated with Eq. B6.

ion fraction  $\eta_i$  decreases exponentially with increasing ion temperature, as shown in Fig. 4. Details of the passing fraction calculation are included in Appendix B. Hence, the (now fewer) passing ions must be accelerated to higher velocities by a larger potential in order to balance the passing electron current. Lastly, at fixed ion and electron temperature, we observe that the ambipolar potential decreases with increasing  $R$ . This is simply because more electrons are trapped by the mirror field, resulting in a smaller electron passing current.

Notably, the exponential dependence of the ion passing fraction on temperature has important consequences for ion confinement estimates. Although the particle passing fraction asymptotically approaches the oft-quoted neoclassical limit as  $T/\varphi \rightarrow \infty$  (shown by the green dashed line in Fig. 4), this high temperature limit is rarely met in reality because  $\varphi$  is typically comparable to  $T_e$ , being set by the ambipolar condition (Eq. 16 in our case) [39]. Hence, the differences in estimated trapped particle fractions when using the neoclassical estimate versus the results of Fig. 4 can be significant.

For example, the LTX SOL plasma typically has  $T_e = 200$  eV,  $T_i = 40$  eV,  $R = 4$ , and  $\varphi = 0.5 \sim 3T_e = 100 \sim 600$  eV; we therefore estimate ion passing fraction as  $\eta_i \gtrsim 0.8$ . This is in drastic contradiction to the *trapped* fraction of  $0.8 - 0.9$  (i.e.,  $\eta_i \lesssim 0.2$ ) from the neoclassical estimate which uses only the mirror ratio [33]. This trend also holds for a more general SOL plasma with  $T_i \approx T_e$  and low collisionality -  $\eta_i$  will be moderately lower than the above LTX-based estimate, but is still expected to be significantly higher than the neoclassical estimate due to the presence of  $\varphi$ . Hence, we conclude that despite the relatively high mirror ratio of the ST magnetic geometry, the ions in a collisionless SOL are still not mirror-confined, and their main loss mechanism remains direct

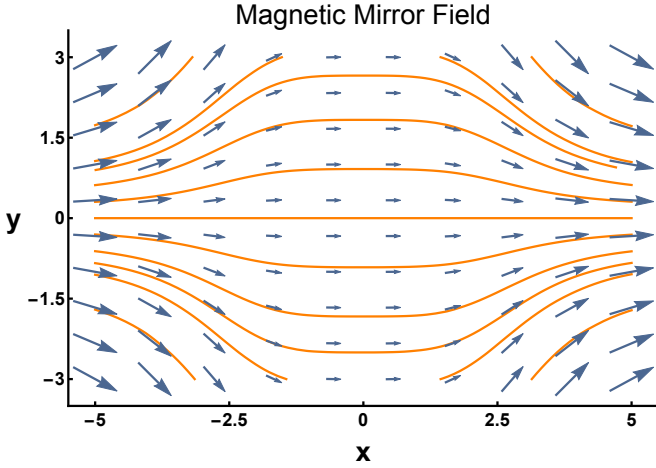


**FIG. 5:** Magnetic mirror geometry used in the presented code benchmarking. The magnetic field lines obtained as the level sets of the stream function  $\psi(x, y)$  [Eq. 17] are shown in orange, while the strength and orientation of the resulting magnetic field [Eqs. 18] is depicted by the blue arrows. For this particular case,  $R = 4$ ,  $\ell = 3$ , and  $B_0 = 3$ .

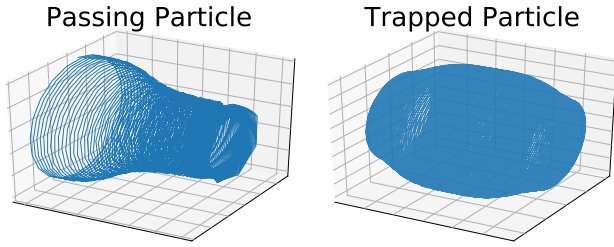


**FIG. 6:** Sample orbits for passing (left) and trapped (right) particles in a magnetic mirror with no imposed electrostatic potential. Particle orbits are traced up to 1 million time steps or until particle hits the edge of computational domain. The first 5,000 steps are shown for the trapped particle.

streaming to the limiters.

### III. BENCHMARKING THE SOLFI FULL ORBIT PARTICLE CODE

SOLFI is a full-orbit Monte-Carlo particle tracer code that aims to simulate the fast ion orbits that traverse both the core and the SOL plasma in a tokamak. It is under development as a possible extension to the NBI code NUBEAM [41] to include SOL effects and aid better understanding of the influence of the SOL on fast particle confinement. That said, the particle tracer code itself is flexible in terms of magnetic geometry (Cartesian or toroidal) and is capable of simulating the dynamics of non-relativistic charged particles of arbitrary species in a variety of magnetic and electric field configurations. Here we benchmark the numerical methods of the code with the test case of particle losses in a collisionless magnetic mirror. (A more complete description of the SOLFI code

will be reported elsewhere.)

#### A. Magnetic field and electric potential profiles of a simple magnetic mirror

To perform the benchmarking, we require an analytical magnetic mirror field in 2-D slab geometry. Recall that if  $\mathbf{B}(x, y)$  is a two-component divergence-free vector field, then it can be described by a scalar stream function  $\psi(x, y)$  such that  $B_x(x, y) = \partial\psi/\partial y$  and  $B_y(x, y) = -\partial\psi/\partial x$ . As such, the level sets of  $\psi(x, y)$  trace out the field lines of  $\mathbf{B}(x, y)$ . For an ideal magnetic mirror, a possible stream function is given by the 2-parameter family

$$\psi(x, y; R, \ell) = B_0 y \left[ \frac{R-1}{(x/\ell)^4 + 1} + 1 \right]^{-1}. \quad (17)$$

The magnetic field components are therefore given as

$$B_x(x, y; R, \ell) = B_0 \frac{1 + (x/\ell)^4}{R + (x/\ell)^4}, \quad (18a)$$

$$B_y(x, y; R, \ell) = -B_0 (R-1) \frac{4(x/\ell)^3 (y/\ell)}{\left[ R + (x/\ell)^4 \right]^2}, \quad (18b)$$

where  $R$  is the mirror ratio and  $\ell$  roughly describes the width of the magnetic well. Notably, along the mirror axis ( $y = 0$ ) the ratio of the magnetic field intensities at midplane and at the mirror end is precisely given by  $R$ , i.e.,  $|\mathbf{B}(\pm\infty, 0; R, \ell)|/|\mathbf{B}(0, 0; R, \ell)| = R$ . Sample field lines are shown in figure 5.

As for the imposed electric potential, it is sufficient for our purposes to choose the spatial profile

$$\phi(x) = \phi_m \cos^6(\pi x/6\ell), \quad (19)$$

where  $\phi_m$  is potential at midplane  $x = 0$ , and the length scale  $\ell$  in Eq. 19 is the same  $\ell$  that occurs in the magnetic field profile in Eq. 18. This specific functional form of  $\phi$  is chosen to ensure that the collection plane  $x = \pm 3\ell$  in our benchmarking study is accessible to all initialized particles (see Sec. II), although we note that it is not necessarily the self-consistent potential field that would result from the particle motion.

The simulation domain is chosen as  $x \in [-3\ell, 3\ell]$  and  $y, z \in [-10\ell, 10\ell]$ , where the magnetic axis is along the  $\hat{x}$  direction. The large size of domain in the perpendicular direction is chosen to allow the perpendicular scale length of the magnetic field to be much larger than the particle Larmor radius, such that all curvature and gradient drifts are negligible and cross field losses do not occur. The choice to have the collection plane at  $x = \pm 3\ell$  is simply because  $|\mathbf{B}(3\ell, 0; R, \ell)|/|\mathbf{B}(0, 0; R, \ell)|$  is satisfactorily close to the (desired) asymptotic mirror ratio  $R$ .

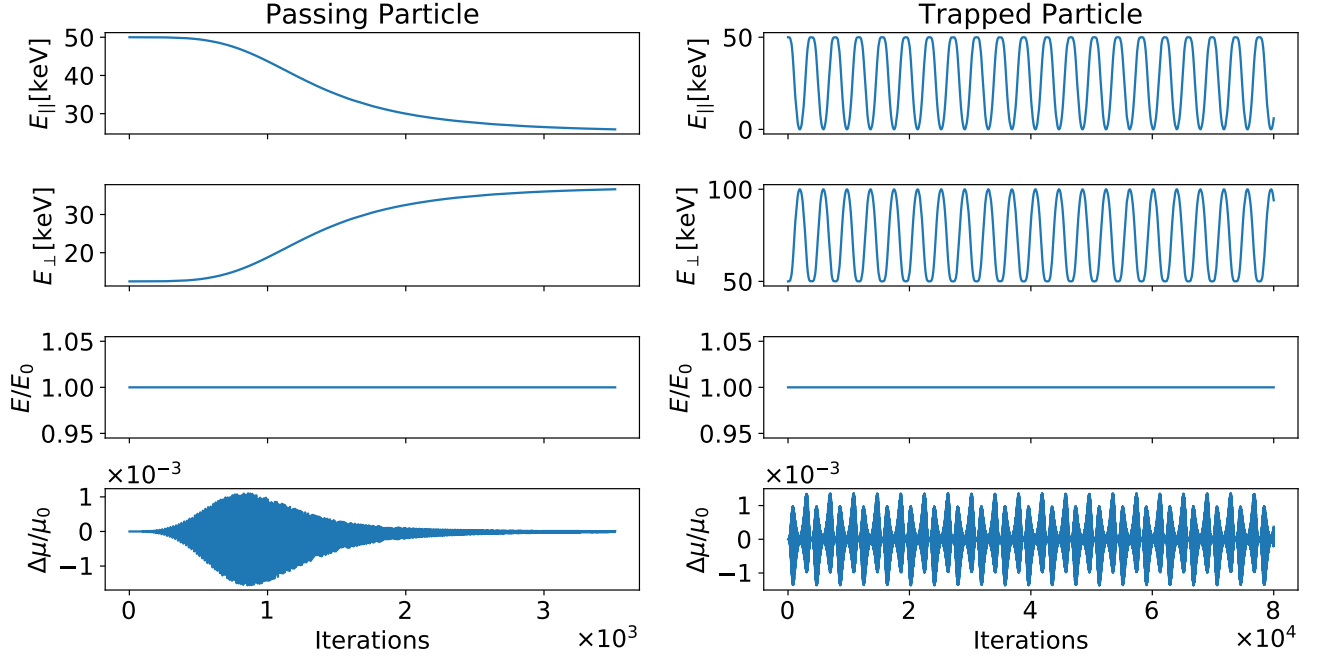


**FIG. 7:** Example time evolution of energy and magnetic moment of a passing particle (left) and trapped particle (right) moving in the magnetic mirror field of Eq. 18 without an imposed electric potential, with energies typical for NBI ions in NSTX-U. The parallel, perpendicular, and total energy as well as the change in the magnetic moment of the particles are shown. The first 20 bounces are shown for the trapped particle. Energy is perfectly conserved as expected, while magnetic moment oscillates around a constant value. Simulations for other energies are qualitatively similar.

### B. Charged particle dynamics

The equations of motion for charged particles is simply the combination of Coulomb and Lorentz force:

$$\frac{d\mathbf{x}}{dt} = \mathbf{v}, \quad (20a)$$

$$m_s \frac{d\mathbf{v}}{dt} = -q_s \frac{d\phi(x)}{dx} \hat{x} + q_s \mathbf{v} \times \mathbf{B}, \quad (20b)$$

where the electrostatic potential is assumed to vary only in the  $\hat{x}$  direction. The equations of motion is numerically integrated with the Boris algorithm [47], which guarantees energy conservation [48]. Examples of passing and trapped particle orbits in the mirror field of Eq. 18 without an electrostatic potential drop are shown in Fig. 6. Figure 7 shows the corresponding time evolution of parallel, perpendicular, and total energy as well as the magnetic moments of the passing and trapped particles with energies similar to those of NBI ions in NSTX-U. It can be seen that while the parallel and perpendicular energies transfer back and forth between bounces, the total energy of the particles are conserved exactly. The magnetic moment is calculated as  $E_{\perp}/B$ , which exhibits small oscillations around a constant value. This small oscillation has been previously explained as the truncation error of the full adiabatic expansion [13], which is an artifact of the simple  $\mu = E_{\perp}/B$  representation and not cause for concern since the oscillation is also bounded.

To verify the passing/trapped boundary of sample particles, a collection of 20,000 particles are launched into the magnetic midplane  $x = 0$  with Maxwellian velocity distribution. The particles are pushed up to 1 million timesteps, with  $\sim 5$  steps per Larmor period. Particles that reach the mirror end at  $x = \pm 3\ell$  are flagged as “passing”, or “trapped” otherwise. Figure 8 shows the *initial* energy space distribution of the test particles and whether they are trapped or lost, with and without the ambipolar potential that satisfies Eq. 16. The simulated passing boundaries show excellent agreement with theoretical predictions. (Simulations were performed for a range of thermal plasma parameters, and the results are all qualitatively similar to those presented in Fig. 8.)

We shall now verify that the net passing current indeed vanishes for the ambipolar potential drop  $\varphi$  that satisfies Eq. 16. To calculate the passing current, the parallel velocities of the particles when they reach the mirror end are recorded and then summed. This sum of velocities is proportional to the total passing particle current. Both electron and ion current are calculated as a function of the midplane potential with fixed electron temperature, but varying ion temperature and mirror ratio  $R$ . The resulting current is shown in Fig. 9, where the ion and electron currents are seen to converge as the midplane potential approaches the predicted ambipolar value  $\phi_0$  in all cases.

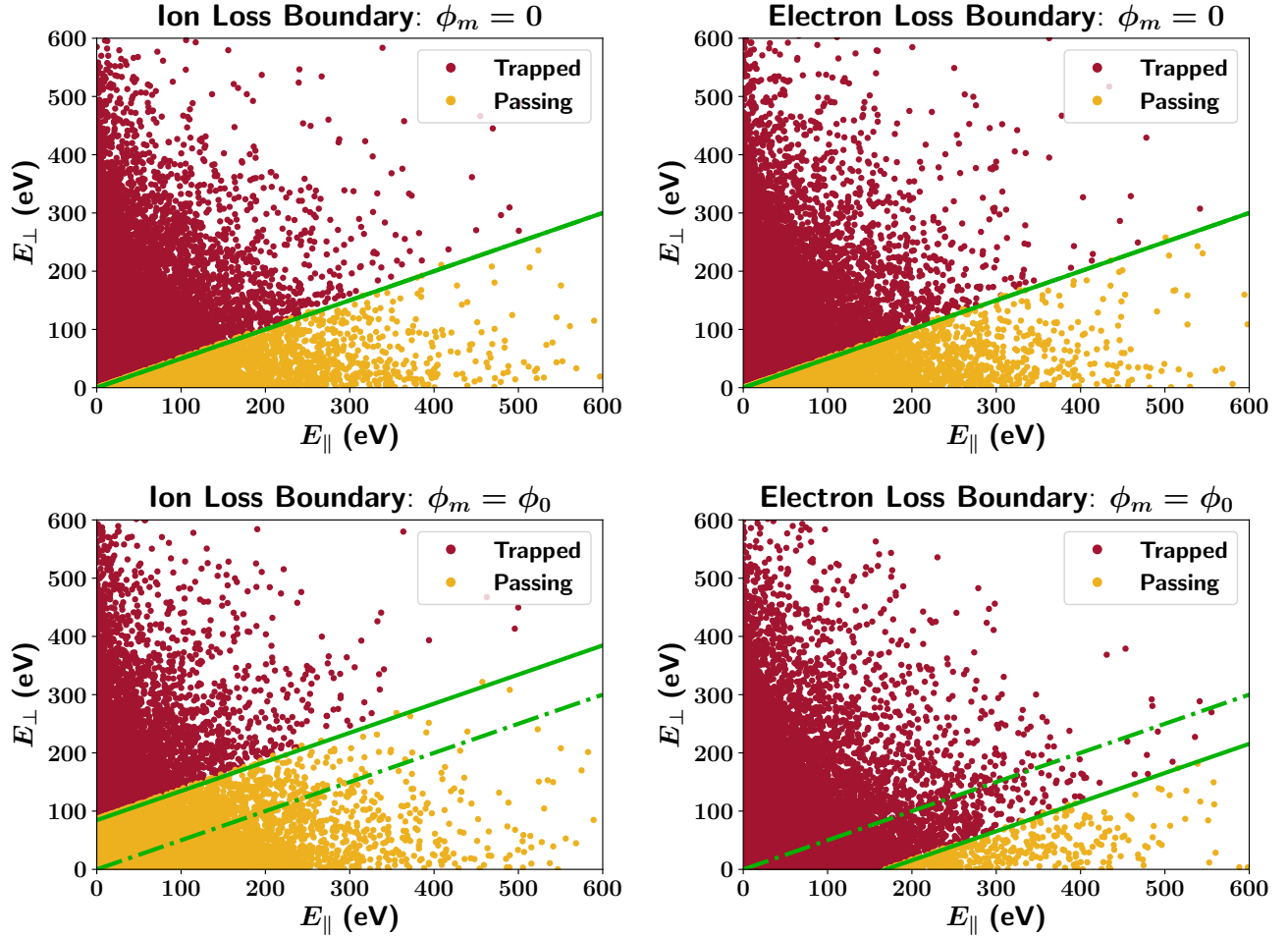


**FIG. 8:** Ion and electron passing boundaries from full-orbit simulations. Particles are initialized according to the Maxwellian distribution of Eq. 9 with LTX-like thermal plasma parameters  $T_i = T_e = 100$  eV. Mirror ratio in this simulation is set to be  $R = 3$ . Each point represents the initial energy-space location of a particle. Ten thousand particles are injected at the midplane and followed for up to 1 million time steps. Dashed green lines are the expected passing boundary in absence of electric potential, whereas solid green lines are the expected loss boundaries with ambipolar potential  $\phi_0$  imposed, where  $\phi_0$  satisfies Eq. 16. The simulated passing boundaries show excellent agreement with predictions. Number of particles is  $N = 20,000$ . Note that simulations performed with NSTX-like thermal plasma parameters  $T_i = T_e \approx 1000$  eV are qualitatively similar and therefore not presented.

#### IV. CONCLUSION

In this paper we present the benchmarking results of the full-orbit Monte Carlo particle code SOLFI in a simple magnetic mirror. The passing particle current and the resulting ambipolar potential are derived analytically and compared to the simulation results, which show excellent agreement. The conservation properties of energy and magnetic moment of the particle tracing algorithm is demonstrated, and example 3D particle orbits are presented. The simulated passing/trapped boundary with and without the ambipolar potential also show excellent agreement with predictions. Overall, the collisionless particle tracing algorithm of SOLFI is consistent with expectations.

The passing particle fraction  $\eta_s$  and associated current

density  $j_s$  in the presence of a electrostatic potential drop  $\varphi$  is also derived. For particle species with relatively low temperatures ( $T/\varphi$  not too large), the passing fraction is exponentially modified by  $\varphi$ . In particular, the thermal SOL ions in STs such as LTX remain untrapped by magnetic mirror field even when collisions are neglected. The exponential dependence of  $\eta_s$  on  $\varphi$  suggests that even in the closed field line regions of tokamak plasmas, a strong electric field may have a significant effect on neoclassical particle confinement.

For example, strong radial electric fields are known to exist in the H-mode pedestal as a result of the pressure gradient [49]. The electrostatic potential drop associated with this radial electric field across a trapped ion banana orbit is typically on the order of  $T_i$  [50]. Our results suggest that this electrostatic potential drop could

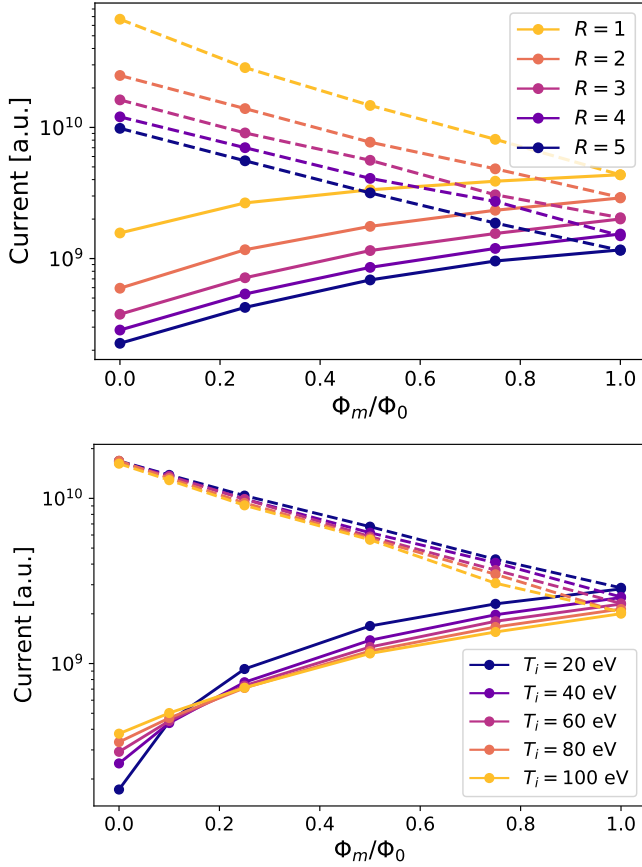


**FIG. 9:** Convergence of electron (dashed lines) and ion (solid lines) passing current as the midplane potential  $\phi_m$  approaches the theoretical value  $\phi_0$  for the ambipolar potential that satisfies Eq. 16. (top) Mirror ratio  $R$  is varied and  $T_i = T_e$ . (bottom)  $T_i$  is varied,  $T_e = 100$  eV and  $R = 3$ . The passing current is calculated as the sum of particle velocities for the passing particles as they escape the magnetic mirror. Note that 20,000 particles are used to obtain each data point.

have strong consequences for neoclassical processes where trapped particles play a significant role, such as the bootstrap current [50, 51]. These effects along with fast ion transport in tokamak edge plasmas will be the subject of further studies. Numerical algorithms for collisions of the tracer particles with a thermal plasma background are being developed in parallel [52, 53] and will be included in future versions of SOLFI, which will allow for more realistic predictions and aid physics understandings.

## ACKNOWLEDGEMENTS

The authors would like to acknowledge Elijah Kolmes and Ian Ochs for helpful conversation and general encouragement. X Zhang would like to thank Leonid Zakharov, Richard Majeski, and Nathaniel Fisch for inspiration and helpful guidance. This work is supported by US DOE

contract DE-AC02-09CH11466.

## DATA AVAILABILITY

The data that support the findings of this study are available from the corresponding author upon reasonable request.

## Appendix A: Derivation of Eq. 14

Here we derive Eq. 14 from Eq. 13. Let us first consider the inner integration over  $w$ , which has the general form

$$\int_0^{\sqrt{a}} dw w \sqrt{a - w^2} e^{-w^2} = e^{-a} \int_0^{\sqrt{a}} dt t^2 e^{t^2}, \quad (\text{A1})$$

where we transformed the integration variable from  $w$  to  $t \doteq \sqrt{a - w^2}$ . Note that  $a = (u^2 + X)/(R - 1)$  in terms of Eq. 13. Integration by parts then yields

$$\begin{aligned} e^{-a} \int_0^{\sqrt{a}} dt t^2 e^{t^2} &= \frac{t}{2} e^{t^2 - a} \Big|_0^{\sqrt{a}} - \frac{1}{2} e^{-a} \int_0^{\sqrt{a}} dt e^{t^2} \\ &= \frac{\sqrt{a}}{2} - \frac{1}{2} \mathcal{D}(\sqrt{a}), \end{aligned} \quad (\text{A2})$$

where  $\mathcal{D}(z)$  is the Dawson function [45, 46], defined as

$$\mathcal{D}(z) = e^{-z^2} \int_0^z dt e^{t^2}. \quad (\text{A3})$$

Let us first consider the case when  $X > 0$ . Substituting Eq. A2 into Eq. 13 yields

$$\begin{aligned} \mathcal{I}(X > 0; R) &= \int_0^\infty du \frac{\sqrt{u^2 + X}}{2} e^{-u^2} \\ &\quad - \frac{\sqrt{R-1}}{2} \int_0^\infty du \mathcal{D}\left(\sqrt{\frac{u^2 + X}{R-1}}\right) e^{-u^2}. \end{aligned} \quad (\text{A4})$$

The variable transformation  $u = \sqrt{X} \sinh(t/2)$  then yields

$$\begin{aligned} \mathcal{I}(X > 0; R) &= \int_0^\infty dt \frac{X [\cosh(t) + 1]}{8} \exp\left[\frac{X}{2} - \frac{X}{2} \cosh(t)\right] \\ &\quad - \frac{\sqrt{X(R-1)}}{4} \mathcal{C}(X; R) \exp\left(\frac{X}{2}\right), \end{aligned} \quad (\text{A5})$$

where  $\mathcal{C}(X; R)$  is defined in Eq. 15a. By recognizing the Sommerfeld integral representation [45, 54]:

$$K_\nu(z) = \int_0^\infty dt \cosh(\nu t) \exp[-z \cosh(t)], \quad (\text{A6})$$

then Eq. A5 can be simplified to the top line of Eq. 14.

Let us next consider the case when  $X < 0$  and Eq. 13 takes the form

$$\begin{aligned} \mathcal{I}(X < 0; R) = & \int_{\sqrt{|X|}}^{\infty} du \frac{\sqrt{u^2 - |X|}}{2} e^{-u^2} \\ & - \frac{\sqrt{R-1}}{2} \int_{\sqrt{|X|}}^{\infty} du \mathcal{D} \left( \sqrt{\frac{u^2 - |X|}{R-1}} \right) e^{-u^2}. \end{aligned} \quad (\text{A7})$$

The variable transformation  $u = \sqrt{|X|} \cosh(t/2)$  then yields

$$\begin{aligned} \mathcal{I}(X < 0; R) = & \int_0^{\infty} dt \frac{X [1 - \cosh(t)]}{8} \exp \left[ \frac{X}{2} + \frac{X}{2} \cosh(t) \right] \\ & - \frac{\sqrt{X(1-R)}}{4} \mathcal{S}(|X|; R) \exp \left( \frac{X}{2} \right), \end{aligned} \quad (\text{A8})$$

where  $\mathcal{S}(X; R)$  is defined in Eq. 15b. As before, invoking Eq. A6 simplifies Eq. A8 to the bottom line of Eq. 14.

Finally, let us consider  $X = 0$ . After noting that

$$\int_0^{\infty} du u e^{-u^2} = \frac{1}{2}, \quad (\text{A9})$$

substitution of Eq. A2 into Eq. 13 yields

$$\mathcal{I}(0; R) = \frac{1}{4} - \frac{\sqrt{R-1}}{2} \int_0^{\infty} du \mathcal{D} \left( \frac{u}{\sqrt{R-1}} \right) e^{-u^2}. \quad (\text{A10})$$

By making use of the identity [55]

$$\int_0^{\infty} du \mathcal{D}(au) e^{-bu^2} = \frac{\text{csch}^{-1} \left( \frac{\sqrt{b}}{a} \right)}{2\sqrt{a^2 + b}}, \quad a, b > 0, \quad (\text{A11})$$

one simplifies Eq. A10 to the middle line of Eq. 14.

## Appendix B: Passing particle fraction

Here, we derive the passing particle fraction in an ideal mirror with potential drop  $\varphi$  for the gyrotropic Maxwellian distribution function provided in Eq. 9. By definition, the fraction of passing particles for species  $s$

with respect to all particles with  $v_{||,0} \geq 0$ , denoted  $\eta_s$ , is given when  $q_s \varphi \geq 0$  as

$$\eta_s = \frac{4}{\sqrt{\pi}} \int_0^{\infty} du e^{-u^2} \int_0^{\sqrt{a}} dw w e^{-w^2}, \quad (\text{B1})$$

or when  $q_s \varphi < 0$  as

$$\eta_s = \frac{4}{\sqrt{\pi}} \int_{\sqrt{\frac{|q_s \varphi|}{T_s}}}^{\infty} du e^{-u^2} \int_0^{\sqrt{a}} dw w e^{-w^2}, \quad (\text{B2})$$

where we have introduced  $a \doteq (u^2 + q_s \varphi / T_s) / (R - 1)$ . We readily evaluate

$$\int_0^{\sqrt{a}} dw w e^{-w^2} = \frac{1}{2} - \frac{1}{2} e^{-a}. \quad (\text{B3})$$

Hence, for  $q_s \varphi \geq 0$  we obtain

$$\begin{aligned} \eta_s = & \frac{2}{\sqrt{\pi}} \left\{ 1 - \sqrt{\frac{R-1}{R}} \exp \left[ -\frac{q_s \varphi_s}{T_s (R-1)} \right] \right\} \\ & \times \int_0^{\infty} du \exp(-u^2) \\ = & 1 - \sqrt{\frac{R-1}{R}} \exp \left[ -\frac{q_s \varphi_s}{T_s (R-1)} \right]. \end{aligned} \quad (\text{B4})$$

Note that when  $\varphi = 0$ ,  $\eta_s$  becomes independent of the species temperature  $T_s$ .

By making use of the identity

$$\int_a^{\infty} dx e^{-bx^2} = \frac{1}{2} \sqrt{\frac{\pi}{a}} \text{erfc}(a\sqrt{b}), \quad a, b > 0, \quad (\text{B5})$$

one can show that for  $q_s \varphi < 0$ ,  $\eta_s$  takes the form

$$\begin{aligned} \eta_s = & \text{erfc} \left( \sqrt{\frac{|q_s \varphi|}{T_s}} \right) \\ & - \sqrt{\frac{R-1}{R}} \text{erfc} \left( \sqrt{\frac{|q_s \varphi|}{T_s} \frac{R}{R-1}} \right) \exp \left[ \frac{|q_s \varphi|}{T_s (R-1)} \right]. \end{aligned} \quad (\text{B6})$$

Representative traces of Eq. B4 and Eq. B6 are shown in Fig. 4 of the main text. Clearly, the fraction of passing ions  $\eta_i$  decreases exponentially with increasing temperature. In fact, the passing fraction of both species approach the asymptotic value  $1 - \sqrt{(R-1)/R}$  as the temperature is increased.

- 
- [1] Y.-K. M. Peng and D. J. Strickler, *Nucl. Fusion* **26**, 769 (1986).
  - [2] Y.-K. M. Peng, *Phys. Plasmas* **7**, 1681 (2000).
  - [3] M. Ono and R. Kaita, *Phys. Plasmas* **22**, 040401 (2015).
  - [4] S. M. Kaye, D. J. Battaglia, D. Baver, E. Belova,

- J. W. Berkery, V. N. Duarte, N. Ferraro, E. Fredrickson, N. Gorelenkov, W. Guttenfelder, and G. Z. Hao, *Nucl. Fusion* **59**, 112007 (2019).
- [5] L. G. Eriksson and F. Porcelli, *Plasma Phys. Control. Fusion* **43**, R145 (2001).

- [6] W. W. Heidbrink and G. J. Sadler, *Nucl. Fusion* **34**, 535 (1994).
- [7] P. R. Thomas, P. Andrew, B. Balet, D. Bartlett, J. Bull, B. De Esch, A. Gibson, C. Gowers, H. Guo, G. Huysmans, and T. Jones, *Phys. Rev. Lett.* **80**, 5548 (1998).
- [8] R. V. Budny, J. G. Cordey, TFTR Team, and JET Contributors, *Nucl. Fusion* **56**, 056002 (2016).
- [9] G. Z. Hao, W. W. Heidbrink, D. Liu, M. Podesta, L. Stagner, R. E. Bell, A. Bortolon, and F. Scotti, *Plasma Phys. Control. Fusion* **60**, 025026 (2018).
- [10] D. Liu, W. W. Heidbrink, M. Podesta, G. Z. Hao, D. S. Darrow, E. D. Fredrickson, and D. Kim, *Nucl. Fusion* **58**, 082028 (2018).
- [11] W. Buangam, J. Garcia, T. Onjun, and JET Contributors, *Plasma Sci. Technol.* **22**, 065101 (2020).
- [12] J. Lestz, E. Belova, and N. N. Gorelenkov, *Nucl. Fusion* (2021).
- [13] E. V. Belova, N. N. Gorelenkov, and C. Z. Cheng, *Phys. Plasmas* **10**, 3240 (2003).
- [14] E. V. Belova, E. D. Fredrickson, J. B. Lestz, N. A. Crocker, and NSTX-U Team, *Phys. Plasmas* **26**, 092507 (2019).
- [15] M. A. Van Zeeland, C. S. Collins, W. W. Heidbrink, M. E. Austin, X. D. Du, V. N. Duarte, A. Hyatt, G. Kramer, N. Gorelenkov, B. Grierson, and D. Lin, *Nucl. Fusion* **59**, 086028 (2019).
- [16] M. A. Van Zeeland, L. Bardoczi, J. G. Martin, W. W. Heidbrink, M. Podesta, M. E. Austin, C. Collins, X. Du, V. N. Duarte, M. Garcia-Munoz, and S. Munaretto, *Nucl. Fusion* **61**, 066028 (2021).
- [17] J. Yang, M. Podesta, and E. D. Fredrickson, *Plasma Phys. Control. Fusion* **63**, 045003 (2021).
- [18] D. Kim, M. Podesta, D. Liu, G. Hao, and F. M. Poli, *Nucl. Fusion* **59**, 086007 (2019).
- [19] M. Podesta, L. Bardoczi, C. Collins, N. N. Gorelenkov, W. W. Heidbrink, V. N. Duarte, G. J. Kramer, E. D. Fredrickson, M. Gorelenkova, D. Kim, and D. Liu, *Nucl. Fusion* **59**, 106013 (2019).
- [20] K. G. McClements and E. D. Fredrickson, *Plasma Phys. Control. Fusion* **59**, 053001 (2017).
- [21] M. A. Jaworski, T. Abrams, J. P. Allain, M. G. Bell, R. E. Bell, A. Diallo, T. K. Gray, S. P. Gerhardt, R. Kaita, H. W. Kugel, and B. P. LeBlanc, *Nucl. Fusion* **53**, 083032 (2013).
- [22] V. A. Evtikhin, I. E. Lyublinski, A. V. Vertkov, S. V. Mirnov, V. B. Lazarev, N. P. Petrova, S. M. Sotnikov, A. P. Chernobai, B. I. Khripunov, V. B. Petrov, and D. Y. Prokhorov, *Plasma Phys. Control. Fusion* **44**, 955 (2002).
- [23] Y. Nagayama, *Fusion Eng. Des.* **84**, 1380 (2009).
- [24] T. D. Rognlien, M. E. Rensink, E. Emdee, R. J. Goldston, J. Schwartz, and D. Stotler, *Nucl. Mater. Energy* **18**, 233 (2019).
- [25] M. Poradziński, I. Ivanova-Stanik, G. Pelka, V. P. Ridolfini, and R. Zagórski, *Fusion Eng. Des.* **146**, 1500 (2019).
- [26] M. Ono and R. Raman, *J. Fusion Energy*, 1 (2020).
- [27] E. D. Emdee, R. J. Goldston, J. A. Schwartz, M. Rensink, and T. D. Rognlien, *Nucl. Fusion* **59**, 086043 (2019).
- [28] R. Majeski, H. Kugel, R. Kaita, S. Avasarala, M. G. Bell, R. E. Bell, L. Berzak, P. Beiersdorfer, S. P. Gerhardt, E. Granstedt, T. Gray, C. Jacobson, J. Kallman, S. Kaye, T. Kozub, B. P. LeBlanc, J. Lepson, D. P. Lundberg, R. Maingi, D. Mansfield, S. F. Paul, G. V. Pereverzev, H. Schneider, V. Soukhanovskii, T. Strickler, D. Stotler, J. Timberlake, L. E. Zakharov, and The NSTX and LTX Research Teams, *Fusion Eng. Des.* **85**, 1283 (2010).
- [29] D. K. Mansfield, D. W. Johnson, B. Grek, H. W. Kugel, M. G. Bell, R. E. Bell, R. V. Budny, C. E. Bush, E. D. Fredrickson, K. W. Hill, and D. L. Jassby, *Nucl. Fusion* **41**, 1823 (2001).
- [30] S. V. Mirnov, V. B. Lazarev, S. M. Sotnikov, T-11M Team, V. A. Evtikhin, I. E. Lyublinski, and A. V. Vertkov, *Fusion Eng. Des.* **65**, 455 (2003).
- [31] M. L. Apicella, G. Mazzitelli, V. P. Ridolfini, V. Lazarev, A. Alekseyev, A. Vertkov, R. Zagorski, and FTU Team, *J. Nucl. Mater.* **363**, 1346 (2007).
- [32] H. W. Kugel, M. G. Bell, J.-W. Ahn, J. P. Allain, R. Bell, J. Boedo, C. Bush, D. Gates, T. Gray, S. Kaye, and R. Kaita, *Phys. Plasmas* **15**, 056118 (2008).
- [33] R. Majeski, R. E. Bell, D. P. Boyle, R. Kaita, T. Kozub, B. P. LeBlanc, M. Lucia, R. Maingi, E. Merino, Y. Raiteses, J. C. Schmitt, J. P. Allain, F. Bedoya, J. Bialek, T. M. Biewer, J. M. Canik, L. Buzi, B. E. Koel, M. I. Patino, A. M. Capece, C. Hansen, T. Jarboe, S. Kubota, W. A. Peebles, and K. Tritz, *Phys. Plasmas* **24**, 056110 (2017).
- [34] D. P. Boyle, R. Majeski, J. C. Schmitt, C. Hansen, R. Kaita, S. Kubota, M. Lucia, and T. D. Rognlien, *Phys. Rev. Lett.* **119**, 015001 (2017).
- [35] L. E. Zakharov, N. N. Gorelenkov, R. B. White, S. I. Krashenninnikov, and G. V. Pereverzev, *Fusion Eng. Des.* **72**, 149 (2004).
- [36] S. I. Krashenninnikov, L. E. Zakharov, and G. V. Pereverzev, *Phys. Plasmas* **10**, 1678 (2003).
- [37] X. Zhang, D. B. Elliott, A. Maan, D. P. Boyle, R. Kaita, and R. Majeski, *Nucl. Mater. Energy* **19**, 250 (2019).
- [38] E. D. Emdee, R. J. Goldston, J. D. Lore, and X. Zhang, *Nucl. Mater. Energy* **27**, 101004 (2021).
- [39] P. C. Stangeby, *The plasma boundary of magnetic fusion devices*, Vol. 224 (New York: Taylor and Francis, 2000).
- [40] R. J. Goldston, *Nucl. Fusion* **52**, 013009 (2011).
- [41] A. Pankin, D. McCune, R. Andre, G. Bateman, and A. Kritz, *Comput. Phys. Commun.* **159**, 157 (2004).
- [42] R. Majeski, L. Berzak, T. Gray, R. Kaita, T. Kozub, F. Levinton, D. P. Lundberg, J. Manickam, G. V. Pereverzev, K. Sniekus, V. Soukhanovskii, J. Spaleta, D. Stotler, T. Strickler, J. Timberlake, J. Yoo, and L. Zakharov, *Nucl. Fusion* **49**, 055014 (2009).
- [43] J. E. Menard, S. Gerhardt, M. Bell, J. Bialek, A. Brooks, J. Canik, J. Chrzanowski, M. Denault, L. Dudek, D. A. Gates, N. Gorelenkov, W. Gutfenfelder, R. Hatcher, J. Hosea, R. Kaita, S. Kaye, C. Kessel, E. Kolen, H. Kugel, R. Maingi, M. Mardenfeld, D. Mueller, B. Nelson, C. Neumeyer, M. Ono, E. Perry, R. Ramakrishnan, R. Raman, Y. Ren, S. Sabbagh, M. Smith, V. Soukhanovskii, T. Stevenson, R. Strykowski, D. Stutman, G. Taylor, P. Titus, K. Tresemer, K. Tritz, M. Viola, M. Williams, R. Woolley, H. Yuh, H. Zhang, Y. Zhai, A. Zolfaghari, and the NSTX Team, *Nucl. Fusion* **52**, 083015 (2012).
- [44] J. P. Freidberg, *Plasma Physics and Fusion Energy* (Cambridge: Cambridge University Press, 2010).
- [45] F. W. J. Olver, D. W. Lozier, R. F. Boisvert, and C. W. Clark, *NIST Handbook of Mathematical Functions* (Cambridge: Cambridge University Press, 2010).
- [46] W. H. Press, S. A. Teukolsky, W. T. Vetterling, and B. P. Flannery, *Numerical Recipes*, 3rd ed. (Cambridge:

- Cambridge University Press, 2007).
- [47] J. P. Boris, in *Proc. Fourth Conf. Num. Sim. Plasmas* (1970) pp. 3–67.
  - [48] H. Qin, S. Zhang, J. Xiao, J. Liu, Y. Sun, and W. M. Tang, *Phys. Plasmas* **20**, 084503 (2013).
  - [49] W. X. Wang, F. L. Hinton, and S. K. Wong, *Phys. Rev. Lett.* **87**, 055002 (2001).
  - [50] G. Kagan and P. J. Catto, *Phys. Rev. Lett.* **105**, 045002 (2010).
  - [51] K. Y. Watanabe, N. Nakajima, M. Okamoto, K. Yamazaki, Y. Nakamura, and M. Wakatani, *Nucl. Fusion* **35**, 335 (1995).
  - [52] X. Zhang, Y. Fu, and H. Qin, *Phys. Rev. E* **102**, 033302 (2020).
  - [53] Y. Fu, X. Zhang, and H. Qin, *arXiv preprint arXiv:2010.12920* (2020).
  - [54] G. N. Watson, *A Treatise on the Theory of Bessel Functions*, 2nd ed. (Cambridge: Cambridge University Press, 1966).
  - [55] K. B. Oldham, J. C. Myland, and J. Spanier, *An Atlas of Functions*, 2nd ed. (New York: Springer, 2009).